Sister chromatid separation determines the proliferative properties upon whole-genome duplication via homologous chromosome arrangement

Masaya Inoko[1], Guang Yang[1], Yuki Tsukada[2], and Ryota Uehara[1,3]

[1]Graduate School of Life Science, Hokkaido University, Japan

[2]Department of Biosciences and Informatics, Keio University, Japan

[3]Faculty of Advanced Life Science, Hokkaido University, Japan

Corresponding author:

Ryota Uehara, Faculty of Advanced Life Science, Hokkaido University, Kita 21, Nishi 11, Kita-Ku, Sapporo 001-0021, Japan

E-mail: ruehara@sci.hokudai.ac.jp

Phone: 81-11-706-9238

18 **Significance**

19

20 Whole-genome duplication (WGD), doubling of cellular content through skipping cell division after
21 DNA synthesis, drives cellular diversification in development, aging, tumorigenesis, or evolution.
22 While various mechanisms of WGD are featured in different biological contexts, the potential
23 impacts of differences in WGD mechanisms on resulting cellular properties have been overlooked.
24 Here, we discovered that two major mechanisms of WGD, mitotic slippage and cytokinesis failure,
25 differentially affect proliferative characteristics of post-WGD cells through their contrasting
26 intracellular reorganizations. Mitotic slippage, occurring with inefficient sister chromatid
27 separation, led to a skewed homologous chromosome distribution compared to cytokinesis failure,
28 fueling lethal chromosome loss by non-random chromosome segregation immediately after WGD.
29 Our findings provide insights into the context-dependent preferences for WGD mechanisms.
30

Summary

Whole-genome duplication (WGD) of diploid cells triggers various cell fates, such as cell death, cell cycle arrest, and proliferation with chromosome instability, contributing to broad bioprocesses, including differentiation, tumorigenesis, or aging. However, factors determining the post-WGD cell fates remain largely unknown. In this study, we found that cytokinesis failure (CF) and mitotic slippage (MS), two major routes of WGD induction, differentially affected post-WGD viability and proliferation in human cells. Quantitative live imaging revealed poorer survivability of cells upon multipolar chromosome segregation at the first mitosis after MS than CF. Chromosome-specific labeling showed that the inefficient sister chromatid separation upon MS caused more skewed homologous chromosome distribution than CF. The skewed homologue distribution frequently led to physical isolation (> 10 μm) of the centrosomes from all homologous centromeres, hindering these centrosomes from capturing any of these homologues. The difference in the frequency of this nullisomic chromosome segregation between MS and CF at least partially explained their difference in the viability of the subsequent daughter cells. Moreover, artificial separation of sister chromatids upon MS improved the evenness of homologue distribution, suppressed nullisomic homologue segregation in the following mitosis, and significantly restored the viability of their daughter cells. These results demonstrate the geometric arrangement of homologous chromosomes, defined by the presence or absence of sufficient sister chromatid separation upon WGD, as a key factor determining the proliferative characteristics of subsequent progenies. Our findings would provide a clue to understanding the route-dependent outcomes of WGD in cell fate determination in different bioprocesses.

54 **Introduction**

55

56 Whole-genome duplication (WGD) contributes to the progression of broad biological phenomena
57 such as development, aging, cancer, and evolution (1-3). Different cellular processes lead to WGD,
58 causing various cellular outcomes, including cell death, differentiation, senescence, or proliferation
59 with genome instability (4-6). The complexity and diversity of causes and effects of WGD make it
60 challenging to specify key factors affecting the characteristics of WGD cells. Nevertheless,
61 identification of such factors is important for understanding the mechanisms of the different
62 biological phenomena mentioned above.

63

64 Cell division failure is a critical cause of WGD in both physiological and pathological processes.
65 There are two main types of cell division failure, cytokinesis failure (CF) and mitotic slippage (MS),
66 leading to WGD (6). CF occurs through defects in dividing the cytoplasm after normal chromosome
67 segregation, forming a binucleated cell that contains two diploid nuclei. Besides spontaneous errors,
68 physiological CF occurs in specific cell types in different tissues, such as hepatocytes,
69 cardiomyocytes, or mammary epithelial cells (7-9). In case of hepatocytes, developmentally
70 programmed suppression of cytokinesis factors mediates the progression of WGD (8). Cancer cells
71 also undergo frequent CF, which is explained, at least in part, by oncogene-mediated suppression of
72 cytokinesis factors (10, 11).

73

74 MS is the premature exit from mitosis without chromosome segregation, resulting in a mononucleated
75 cell that contains a single tetraploid nucleus (6). Chromosome capture by spindle microtubules is a
76 stochastic, error-prone process, and spontaneous defects in bipolar spindle formation cause a risk of
77 chromosome segregation failure. Normally, defects in bipolar kinetochore-microtubule attachment
78 block silencing of the spindle assembly checkpoint (SAC), which arrests mitotic progression until the

defects are resolved. Suppression of SAC through loss-of-function of its components or attenuation of cdk1-dependent maintenance of the mitotic state lets cells escape mitotic arrest, even without completing bipolar kinetochore-microtubule attachment (12). The premature mitotic exit, if occurring without spindle assembly, results in WGD with a single nucleus (12-14). Various cancer cells manifest altered expression of SAC components, resulting in attenuated SAC function (15-18). Similarly, cancer cells with low cdk1 activity show poor ability to undergo mitotic arrest, which is linked to their proneness to MS upon anticancer drug treatment (19). Moreover, overexpression of v-Src oncogene induces MS by suppressing cdk1 activity (20). In contrast to CF, physiological MS has been found in limited cases, such as megakaryocyte formation or DNA-damage-induced keratinocyte differentiation (21, 22). Therefore, while CF and MS both result in WGD, their cellular causes, geometric features, and prevalence in biological contexts are different. However, it remains largely unknown whether CF and MS differentially affect post-WGD cell fates.

Several factors have been found to determine post-WGD cell fates. The p53 signaling pathway is the most studied mechanism, which is activated upon WGD and mediates cell cycle arrest, senescence, or apoptosis during interphase immediately after WGD (23). Upon WGD, the centrosome number doubles, which induces inhibition or cleavage of Mdm2 to stabilize p53 through the activation of the Hippo signaling pathway or the PIDDosome multiprotein complex, respectively (24, 25). On the other hand, overexpression of cyclin D oncogene allows WGD cells to overcome the p53-mediated cell cycle arrest and proliferate (26, 27). Moreover, proliferative post-WGD subclones established from p53-proficient diploid cell lines frequently manifest altered p53 signaling (28), possibly enabling them to override the WGD-linked anti-proliferative mechanisms.

Once cells evade cell cycle arrest or death immediately after WGD, they enter the first mitosis with 4 centrosomes. A part of these WGD cells cluster the excess centrosomes to form “pseudo-bipolar”

104 spindles to conduct bipolar chromosome segregation (29-31). Moreover, the pseudo-bipolar spindle
105 formation with asymmetric centrosome clustering (i.e., segregating in 1:3 ratio) contributes to
106 efficient removal of the excess centrosomes in their progenies (32). Otherwise, WGD cells form
107 multipolar spindles with the excess centrosomes, driving chromosome segregation into more than 2
108 daughter cells. Early studies by Boveri proposed that multipolar chromosome segregation occurs in
109 a stochastic fashion, leading to drastic chromosome copy number alterations (33). A substantial
110 proportion of such multipolar daughters are supposed to die due to their lethal karyotypes. On the
111 other hand, the remaining survivors potentially contribute to clonal evolution of WGD progenies with
112 gross aneuploidy, hence driving phenotypic diversification (34-36). Indeed, a frequent multipolar cell
113 division results in the formation of aneuploid progenies after physiological WGD in hepatocytes (37).
114 Therefore, the quality of multipolar chromosome segregation in the early post-WGD phase can be
115 one of the critical factors determining the characteristics of post-WGD cell populations. Importantly,
116 most of the above-mentioned post-WGD alterations (i.e., the excess centrosome gaining, p53
117 signaling, or multipolar spindle defects) occur in common either after CF or MS (25, 27), having
118 drawn no attention to possible impacts of differences in the route of WGD induction.
119
120 In this study, we systematically compared post-WGD cell proliferation after MS or CF using HCT116,
121 a near-diploid human cell line commonly used in ploidy comparative studies (38).
122

Results

MS-derived WGD cells are less proliferative than CF-derived ones

To gain insight into potential differences in properties of WGD cells derived from different types of cell division defects, we compared cell proliferation following pharmacological induction of MS or CF in HCT116. MS-derived WGD (MS-WGD, hereafter) was induced by arresting cells at prometaphase by nocodazole shake-off, followed by co-treating nocodazole and a cdk1 inhibitor RO3306 for mitotic exit without spindle formation (Fig. 1A). CF-derived WGD (CF-WGD) was induced by removing nocodazole from the above prometaphase-arrested cells, and subsequently treating cytochalasin B (Fig. 1A). These compounds were thoroughly washed out after 2-h treatment. MS- and CF-WGD induction resulted in equivalent increases in DNA content (SI Appendix, Fig. S1A and B). Efficiency of MS- or CF-WGD induction, assessed by possession of the excess centrosomes, was 85% or 82%, respectively (SI Appendix, Fig. S1B and C). As expected, most MS- or CF-WGD cells had a single nucleus or two nuclei, respectively (Fig. 1B and C).

We first attempted to evaluate the survival and proliferation of post-WGD cells using flow cytometry after bulk cell culture. However, with this approach, the initially contaminated non-WGD diploid population rapidly dominated the culture within several days, precluding precise evaluation of polyploid cell growth (SI Appendix, Fig. S1D). To avoid this issue, we adopted the colony-counting assay under limited dilution after WGD induction (Fig. 1D). For this, the WGD-induced cells were seeded at 2,000 cells/well in a 6-well culture dish. Cells forming colonies after 8- or 9-d culture were stained with Hoechst 33342 to quantify DNA content distributions in individual colonies using fluorescence microscopy (Fig. 1D and E). Histograms of DNA content in most colonies showed typical cell cycle distributions with G1 and G2/M peaks, indicating their proliferative state (Fig. 1E

148 and Supplemental material S1). Ploidy levels estimated from G1 DNA contents of individual
149 subclones (normalized by the average DNA content in diploid control colonies) distributed in a
150 bimodal fashion, peaking at either near-diploid or polyploid (> 3 C) (Fig. 1F). For the following
151 reason, these near-diploid subclones were likely originated from the cells that escaped WGD
152 induction: Based on the WGD induction rates (SI Appendix, Fig. S1C), about 50-300 out of 2,000
153 cells were assumed to remain diploid (i.e., escaping WGD induction) when seeded after WGD
154 induction. When equivalent numbers of untreated diploids were seeded, we obtained colony counts
155 roughly matching those after the aforementioned WGD induction (SI Appendix, Fig. S1E). Therefore,
156 we excluded these near-diploid colonies and quantified the number of polyploid colonies to assess
157 post-WGD cell proliferation (Fig. 1G). We found that CF-WGD cells reproducibly formed
158 significantly more polyploid colonies compared to MS-WGD cells (Fig. 1G), indicating that the two
159 WGD routes have distinct effects on subsequent cell proliferation. Since this "context-dependent"
160 difference in post-WGD cell proliferation was novel, we decided to address the cellular processes
161 differentially affected between MS- and CF-WGD cells.
162
163 **Poorer survivability of MS-WGD cells through multipolar chromosome segregation at the first**
164 **mitosis**
165
166 The significantly lower number of colonies formed after MS-WGD than CF-WGD indicates that
167 earlier processes of cell proliferation were more severely compromised in the former. We addressed
168 this possibility by live-imaging histone H2B-mCherry as a chromosome marker to investigate the
169 progression and fates of subsequent interphase and mitosis after MS- or CF-WGD (Fig. 2A and B).
170 A substantial proportion of cells completed the first interphase and entered mitosis after MS- or CF-
171 WGD induction (81% or 80%, respectively), while the remaining cells stayed in interphase or died
172 (SI Appendix, Fig. S2A). The relatively efficient mitotic entry indicates that the p53-mediated

173 mechanism, which arrests the cell cycle after WGD or cytochalasin treatment (24, 27, 39), is less
174 stringent in the HCT116 cellular background. Indeed, unlike non-cancer p53-proficient hTERT-RPE1,
175 HCT116 failed in timely upregulating p21, the primary mediator of cell cycle arrest in the p53
176 pathway, despite an increase in p53 expression after WGD (SI Appendix, Fig. S2B, C, and Supporting
177 text 1). Moreover, the mitotic stopwatch, which blocks cell cycle depending on the degree of the
178 previous mitotic delay (40), was inactive in HCT116, resulting in no difference in first cell cycle
179 length between MS- and CF-WGD cells (SI Appendix, Fig. S2D-I, and Supporting text 1). These data
180 excluded the progression of the first interphase as a possible cause of the difference in proliferative
181 capacity between MS- and CF-WGD.
182
183 We next investigated possible differences in the progression of the first mitosis. In the above live-
184 imaging, diploids that escaped WGD induction were distinguished from WGD cells based on nuclear
185 area immediately before mitotic entry and excluded from the analyses (SI Appendix, Fig. S3A).
186 Because of the excess centrosomes gained upon WGD, either MS- or CF-WGD cells suffered an
187 equivalently high frequency of multipolar chromosome segregation with no difference in mitotic
188 duration (89% and 86%, respectively; Fig. 2B, C, SI Appendix, Fig. S3B, and C). We analyzed
189 patterns of these multipolar chromosome segregations. At each event of the first mitosis, the nuclear
190 H2B-mCherry signal was segregated into daughter cells (F1 cells, hereafter) at the ratio that
191 recapitulated those measured by Hoechst 33342 (SI Appendix, Fig. S3D and E). Therefore, assuming
192 that P0 cells had 8 C DNA content at the first mitosis after WGD, we estimated the DNA content of
193 each F1 cell using the H2B-mCherry segregation ratio (Fig. 2D). We noticed that a substantial F1 cell
194 proportion became multinucleated presumably because of incomplete cytokinesis (Fig. 2B, SI
195 Appendix, Fig. S3B, and F), consistent with a previous report (36). Therefore, we separately analyzed
196 these multinucleated F1 populations from the mononucleated ones. Reflecting the stochastic nature
197 of multipolar division, DNA contents were heterogeneous among individual cells (Fig. 2E). DNA

198 contents in mononucleated F1 cells from bipolar, tripolar, or tetrapolar chromosome segregation were
199 on average 4.0, 2.7, or 2.1 C, respectively, both in MS- and CF-WGD (Fig. 2E). DNA contents in F1
200 cells multinucleated after tripolar or tetrapolar chromosome segregation were on average >5.0, or 3.9
201 C, both in MS- and CF-WGD (Fig. 2E). Therefore, either reduction in the segregation polarity or
202 multinucleation contributed to increasing DNA contents in F1 cells.
203
204 Next, we analyzed F1 cell fates, categorized as "divided" (entered the subsequent mitosis), "arrested"
205 (stayed alive without cell division for more than 36 h), or "died" (underwent cell death during the F1
206 cell cycle; Fig. 2E, SI Appendix, Fig. S3G, and H). MS-WGD produced significantly fewer "divided"
207 F1 progenies than CF-WGD (SI Appendix, Fig. S3H). CF-WGD F1 cells gained a significantly higher
208 chance of viability (judged by the frequency of "divided" cells) when they obtained higher DNA
209 contents (Fig. 2F). Consistent with this trend, either the reduction in chromosome segregation polarity
210 or daughter cell multinucleation resulted in higher F1 cell viability (Fig. 2G and SI Appendix, Fig.
211 S3I). Whereas the viability of MS-WGD F1 cells also increased with higher DNA contents, that with
212 1.5-3.5 C DNA contents was significantly lower in MS-WGD than in CF-WGD (Fig. 2F). Similarly,
213 the viability of tripolar chromosome segregation-derived MS-WGD F1 cells was significantly lower
214 than that of CF-WGD F1 cells (Fig. 2G). This result indicates that cells are less tolerant of a reduction
215 in DNA content following multipolar chromosome segregation after MS-WGD than after CF-WGD.
216
217 **Non-random chromosome segregation causes frequent nullisomy after MS-WGD**
218
219 We next addressed the reason for the poorer viability of MS-WGD cells than CF-WGD cells after
220 multipolar chromosome segregation at the first mitosis. For this, we compared patterns of multipolar
221 chromosome segregation at the first mitosis by labeling specific homologous chromosomes using
222 dCas9-EGFP with a specific single-guide RNA (sgRNA) targeting chromosome 9 pericentromere

223 loci (C9-1) (41) (Fig. 3A). The C9-1 labeling was in good agreement with that of a chromosome 9
224 pericentromere-specific FISH probe (SI Appendix, Fig. S4A). We also labeled chromosomes and the
225 centrosomes with H2B-mCherry and EGFP-GCP3, respectively (Fig. 3A and SI Appendix, Fig. S4B;
226 C9-1 and the centrosomes were readily distinguished by their size and relative location to
227 chromosomes).
228
229 We found a prominent variation in the number of C9-1 foci per chromosome mass during multipolar
230 chromosome segregation in both WGD conditions (SI Appendix, Fig. S4C). However, we observed
231 nullisomic chromosome masses devoid of C9-1 focus significantly more frequently after MS-WGD
232 than after CF-WGD (8.6% or 2.9% upon tripolar segregation and 18% or 9.9% upon tetrapolar
233 segregation after MS- or CF-WGD, respectively; Fig. 3B and SI Appendix, Fig. S4C). Nullisomic
234 chromosome masses were also more frequent after MS-WGD than CF-WGD, when chromosome 1
235 or 17 was labeled by FISH (Fig. 3C-F). Moreover, we observed a similar extent of increase in
236 nullisomic segregation when MS-WGD was induced by the transient co-inhibition of a mitotic kinesin,
237 Eg5, and Mps1 kinase (SI Appendix, Fig. S4D; to suppress SAC with monopolar spindle formation).
238 A similar trend of MS-WGD-linked increase in nullisomic segregation was also observed in hTERT-
239 RPE1 cells (SI Appendix, Fig. S4E-G; p53 was depleted by RNAi to allow entry into the first mitosis
240 after WGD). Therefore, MS-WGD led to more frequent nullisomic segregation regardless of
241 chromosome species, the means of MS induction, or the cellular backgrounds we tested.
242
243 Nullisomy of any chromosome species most likely results in death in the F1 generation. Therefore,
244 we theoretically estimated F1 cell viability as the frequency of cells with at least one copy of all
245 chromosome species (Fig. 3G and H). In this estimation, we assumed that the probability of nullisomy
246 formation for all chromosome species was equivalent to that for chromosome 9 (Fig. 3B; see
247 *Discussion* on limitations of the simplified assumption). We estimated F1 viability in either situation

248 i) where the observed chromosome mass was segregated into a mononucleated daughter (Fig. 3G),
249 or ii) where two masses were segregated into a binucleated daughter (Fig. 3H; see Materials and
250 methods for details). The estimated viability of mononucleated F1 cells was in good agreement with
251 the empirical value in the live-imaging analysis for both MS-WGD and CF-WGD (Fig. 3G). The
252 theoretical estimation also recapitulated the drastic increase in F1 cell viability upon their binucleation,
253 though it tended to overestimate the trend (Fig. 3H). These results suggest that the proneness of MS-
254 WGD-derived F1 cells to nullisomy, at least in part, explains their poorer survivability after
255 multipolar chromosome segregation. In a previous theoretical estimation in human WGD cells, 75%
256 or 23% of F1 cells avoided nullisomy of any homologs upon tripolar or tetrapolar segregation,
257 respectively, assuming that all chromosomes were randomly segregated (32). The estimated values
258 were closer to those observed after CF-WGD (Fig. 3G), indicating that the homologous chromosome
259 segregation occurred in a non-random manner after MS-WGD.
260
261 **MS-WGD causes skewed homologous chromosome distribution at the entry into the first**
262 **mitosis**
263
264 We next addressed why nullisomic chromosome segregation occurred more frequently at the first
265 mitosis after MS-WGD than CF-WGD. MS- and CF-WGD cells showed lagging chromosomes or
266 chromosome bridges to the same extent (SI Appendix, Fig. S4H-M), ruling out differences in
267 chromosome segregation fidelity as the cause of the difference in nullisomy frequency between these
268 conditions. As another possible factor affecting nullisomy frequency, we next compared the spatial
269 distribution of homologous chromosomes upon the entry into the first mitosis between MS- and CF-
270 WGD cells by imaging C9-1 along with chromosomes, and the centrosomes (Fig. 4A). At this mitotic
271 stage, most WGD cells possessed four C9-1 foci, as sister chromatids had not yet been separated. In
272 CF-WGD cells, two C9-1 foci in each of two nuclei tended to be located distal to each other, resulting

273 in relatively even distributions of the four C9-1 foci (with an average inter-centromere distance of 9.1
274 μm; Fig. 4A, B, and SI Appendix, Fig. S5A). In sharp contrast, in MS-WGD cells, four C9-1 foci
275 from the single nucleus were often distributed pairwise (Fig. 4A). Accordingly, the frequency of
276 "paired C9-1 foci," defined as those with the inter-centromere distance of < 2 μm, was significantly
277 higher after MS-WGD than CF-WGD (Fig. 4B, C, SI Appendix, Fig. S5A, and B). These C9-1 pairs
278 were occasionally located proximally from each other, resulting in an overall shorter inter-centromere
279 distance among all four C9-1 foci in MS-WGD cells (on average 6.1 μm; Fig. 4B and SI Appendix,
280 Fig. S5A). We also quantified the angles between each two C9-1 foci with regard to the centroid of
281 the whole-chromosome mass (Fig. 4D). The angles were significantly smaller in MS-WGD than in
282 CF-WGD cells (Fig. 4D), reflecting more skewed configurations of homologous centromeres in the
283 former condition.
284
285 Using the above images, we also analyzed spatial coordination between each C9-1 foci and the
286 centrosomes. Four centrosomes had already been separated in most MS- and CF-WGD cells around
287 NEBD, often flanking the chromosome masses from their opposite sides (Fig. 4A and SI Appendix,
288 Fig. S5C). Reflecting the difference in the skewedness of C9-1 distribution, the distance from each
289 centrosome to the closest C9-1 focus was significantly larger with higher deviation in MS-WGD than
290 in CF-WGD cells (7.0 μm or 5.4 μm in MS- or CF-WGD cells, respectively; Fig. 4E, F, and SI
291 Appendix, Fig. S5D). Accordingly, we observed "isolated centrosomes" located extremely far (> 10
292 μm) from any of C9-1 foci more frequently in MS-WGD than in CF-WGD cells (Fig. 4E and G). We
293 also observed the skewed centromere distribution with the frequent centrosome isolation in MS-WGD
294 induced by Eg5 and Mps1 co-inhibition (SI Appendix, Fig. S5A-F). These data collectively
295 demonstrate that MS-WGD and CF-WGD differentially impact the geometry of the first mitosis, with
296 the former introducing more skewed homologous chromosome distributions relative to the
297 centrosomes.

298

299 **Geometric isolation of centrosomes from all homologues drives nullisomic chromosome**
300 **segregation after MS-WGD**

301

302 Distally placed centrosomes may be less likely to capture any homologous centromeres, possibly
303 explaining the frequent nullisomy after MS-WGD. To test this idea, we traced C9-1 foci and the
304 centrosomes from entry into the first mitosis through anaphase after MS-WGD using live imaging
305 (Fig. 5A and SI Appendix, Movie S1). Following the centrosome separation starting before NEBD
306 (SI Appendix, Fig. S6A), spatial coordination between C9-1 foci and the centrosomes drastically
307 changed around NEBD (Fig. 5A). As a result, the distance between each C9-1 focus and each
308 centrosome became highly deviated around NEBD (SI Appendix, Fig. S6B), which was consistent
309 with the above observation (Fig. 4E, F, and SI Appendix, Fig. S5D). During chromosome congression
310 at prometaphase, the initial positions of C9-1 foci around the NEBD were well transmitted to their
311 positions within the aligned metaphase plate (Fig. 5A and SI Appendix, Fig. S6C), consistent with a
312 previous observation in normal mitosis (42). At anaphase onset, each C9-1 focus split into two sister
313 foci. Each of these sister foci was segregated toward one of the four centrosomes, enabling us to
314 identify the centrosomes that captured individual sister chromatids in the early mitotic phase (Fig. 5A
315 and SI Appendix, Fig. S6B). Using this information, we compared distances from C9-1 foci to the
316 centrosomes that captured these foci with those to the centrosomes that did not capture these foci (Fig.
317 5B). The former were significantly shorter than the latter from NEBD to the late prometaphase (Fig.
318 5B). We also analyzed relationship between the C9-1-centrosome distance at NEBD with the
319 frequency of the subsequent capturing of the C9-1 focus by the centrosome (Fig. 5C). A centrosome
320 captured a C9-1 focus at the frequency of >75% when their distance was ≤ 10 μm at NEBD, while
321 the frequency became less than 50% when the distance was > 10 μm (Fig. 5C). Therefore, the initial
322 proximity of the centrosomes to each centromere was linked to a higher chance of their capturing,

323 potentially determining the pattern of subsequent homologue segregation.

324

325 To gain further insight into the possible relationship between early centrosome-centromere
326 arrangement and the subsequent formation of nullisomy, we analyzed the time course of the distance
327 from each centrosome to its closest C9-1 focus (Fig. 5D). The centrosomes that did not capture any
328 C9-1 foci located significantly more distant from their closest C9-1 focus (on average 10 μm, at
329 NEBD) than those capturing at least one C9-1 focus (6.8 μm; Fig. 5D and E). The frequency for a
330 centrosome to fail to capture any C9-1 foci (nullisomic segregation) drastically increased when the
331 distance from the centrosome to the closest C9-1 focus was more than 10 μm at NEBD (Fig. 5F). The
332 same trend was also observed in a live imaging analysis of CF-WGD cells (SI Appendix, Fig. S6D).
333 Consistent with these quantitative data, visual comparisons of C9-1 and centrosome locations
334 between NEBD and anaphase showed the trend that the centrosomes initially located at the area
335 devoid of C9-1 focus failed to capture any C9-1 foci at the subsequent anaphase (Fig. 5A and SI
336 Appendix, Fig. S6C). These results suggest that the initial centrosome-centromere distance is a key
337 determinant of subsequent nullisomy formation.

338

339 We reasoned that, if the above assumption was correct, the frequency of nullisomic homologue
340 segregation could be well predicted by the centrosome-centromere distance around NEBD (Fig. 5F).
341 Indeed, the frequency of the nullisomic homologue segregation, which was predicted based on the
342 distance between each centrosome and its closest C9-1 focus around NEBD, well matched with those
343 obtained by experiments either in MS- or CF-WGD (Fig. 5G, see also Fig. 3B; Materials and methods
344 for details). These data collectively support the idea that the proneness of MS-WGD cells to
345 nullisomic homologue segregation is mainly attributed to the skewed homologue distribution at the
346 entry into the first mitosis.

347

348 **Forced sister chromatid separation in the MS-WGD time window suppresses subsequent**
349 **nullisomic chromosome segregation**
350
351 We wished to further address the causality between the skewed homologue distribution and the
352 frequent nullisomic homologue segregation after MS-WGD. To investigate this, we traced C9-1 foci
353 during MS-WGD to determine how homologue distribution became skewed (SI Appendix, Fig. S7A).
354 Live-imaging revealed that, while < 22% (6 out of 28) sister foci separated by a short distance (> 2
355 μm) during MS-WGD, the rest (22 out of 28) failed to separate to a detectable degree (SI Appendix,
356 Fig. S7A and B). As a result, the distance between sister C9-1 foci remained on average 1.3 μm at the
357 time the cells exited mitosis (SI Appendix, Fig. S7C).
358
359 Inefficient chromatid separation during MS-WGD may skew homologue distribution and limit the
360 evenness of their capturing during the subsequent mitosis. To directly test this idea, we attempted to
361 induce precocious sister chromatid separation by depleting RAD21, a cohesin subunit, during MS-
362 WGD. To avoid pleiotropic damage caused by long-term loss-of-function of cohesin, we employed
363 the auxin-inducible degron 2 (AID2) technology to deplete RAD21 only for a short time window
364 prior to MS-WGD (Fig. 6A) (43). We treated 5-Ph-IAA in RAD21-mAID-Clover (RAD21-mAC)
365 HCT116 expressing OsTIR1(F74G) (43) for 2 h (Fig. 6A), which efficiently degraded RAD21-mAC
366 by the time of MS-WGD induction (SI Appendix, Fig. S7D-F). RAD21-mAC degradation induced
367 precocious sister chromatid disjunction with a significant increase in inter-centromere distance during
368 prometaphase arrest and caused further separation during MS-WGD (Fig. 6B, C, SI Appendix, Fig.
369 S7G-J). As a result, distances between sister C9-1 foci became significantly longer after mitotic exit
370 in RAD21-degraded cells compared to mock-treated control (on average 2.8 μm or 1.5 μm in 5-Ph-
371 IAA- or DMSO-treated condition, respectively; Fig. 6B and C).
372

373 We then removed 5-Ph-IAA, allowing complete restoration of RAD21-mAC expression in the
374 subsequent cell cycle (SI Appendix, Fig. S7E and F). Chromosome spreading showed complete
375 restoration of sister chromatid cohesion at the first mitosis after removing 5-Ph-IAA (SI Appendix,
376 Fig. S7I and J), demonstrating that precocious sister chromatid disjunction was induced only before
377 MS-WGD. Additionally, "diplochromosomes," which form when the sister chromatids do not
378 separate during the previous cell cycle (44), were not prevalent, even in the mock-treated control (SI
379 Appendix, Fig. S7I and Supplemental material S2).
380
381 We next tested the effect of the transient RAD21-mAC depletion before MS-WGD on the subsequent
382 homologue distribution at the first mitosis (Fig. 6D). Along with C9-1, chromosomes and the
383 centrosomes were visualized by DAPI and anti-Cep192 immunostaining, respectively. Distance
384 among C9-1 foci tended to be longer with a significant reduction in "paired C9-1 foci" by the transient
385 RAD21-mAC depletion (Fig. 6D-F). The transient RAD21-mAC depletion also significantly
386 increased the inter-C9-1 foci angles, indicating dispersion of homologous centromeres (Fig. 6G). The
387 distance from each centrosome to its closest C9-1 focus tended to be shorter, with a significant
388 reduction in "isolated centrosomes" by the transient RAD21-mAC depletion (Fig. 6H and I).
389 Moreover, the transient RAD21-mAC depletion significantly reduced the frequency of nullisomic
390 segregation of C9-1 foci, both in tripolar and tetrapolar chromosome segregation (Fig. 6J).
391
392 We also induced precocious sister chromatid separation during MS-WGD by RNAi-mediated
393 depletion of Sororin, a cohesin-stabilizing factor (SI Appendix, Fig. S8A-C) (45, 46). Similar to
394 RAD21-mAC depletion, precocious sister chromatid separation by Sororin depletion led to
395 substantial dispersion of C9-1 foci compared to mock-depleted control at the first mitosis (SI
396 Appendix, Fig. S8D-I), with a significant reduction in the frequency of nullisomic segregation in the
397 subsequent anaphase (SI Appendix, Fig. S8J). The above data collectively demonstrate that

incomplete sister chromatid separation during MS-WGD is the primary cause of uneven distribution of homologous chromosomes after WGD, facilitating the nullisomy-prone multipolar chromosome segregation in the subsequent mitosis.

Forced sister chromatid separation in the MS-WGD time window improved the viability of the F1 generation

Finally, we determined the causality between inefficient sister chromatid separation during MS-WGD and poorer cell survival in the subsequent mitosis. For this, we tested the effects of precocious sister chromatid separation during MS-WGD on subsequent F1 cell viability. Although we initially tried RNAi-mediated Sororin depletion, it resulted in frequent cell cycle arrest before entry into the first mitosis (SI Appendix, Fig. S8K). This result presumably reflects the deleterious effects of consecutive Sororin depletion on the progression of the first cell cycle after MS-WGD, precluding us from using this condition to assess F1 cell viability. Therefore, we next tried transient RAD21-mAC depletion, which avoided the consecutive loss of function of cohesin (SI Appendix, Fig. S7E, F, I, and J). We compared F1 cell viability after MS-WGD with or without the transient RAD21-mAC depletion by live imaging. The transient RAD21-mAC depletion did not affect the efficiency of entry into the first mitosis (SI Appendix, Fig. S9A), suggesting minimal damage during the cell cycle after MS-WGD. The polarity of chromosome segregation at the first mitosis was also unaffected by the transient RAD21-mAC depletion (SI Appendix, Fig. S9B). However, compared to the mock-depleted MS-WGD control, the transient RAD21-mAC depletion significantly increased viable F1 cells with DNA content of 2.5-3.5 C or those generated through tripolar chromosome segregation (Fig. 6K, L, and SI Appendix, Fig. S9C). Total viability of F1 cells was also significantly improved in the transient RAD21-mAC-depleted sample than in the mock-depleted control (SI Appendix, Fig. S9D). These results demonstrate that inefficient sister chromatid separation during MS-WGD limits the viability

423 of their progeny, at least in part, through skewing the distribution of chromosome territories and
424 increasing the chance of nullisomic homologue segregation in the subsequent multipolar cell division.
425
426

427 **Discussion**

428

429 While WGD occurs through multiple cellular processes, it has been unclear whether differences in
430 the WGD route affect the characteristics of the post-WGD cell. We found that the efficiency of sister
431 chromatid separation during WGD defined the spatial arrangement of homologous chromosomes in
432 the subsequent cell cycle. Homologous chromosome arrangement then determined the patterns of
433 multipolar chromosome segregation at the first mitosis, critically affecting the viability of resulting
434 daughter cells. Our findings demonstrate that differences in geometric properties between MS- and
435 CF-WGD cells have a crucial influence on the proliferative characteristics of their progeny.

436

437 We propose the following mechanism of the route-dependent difference in post-WGD cell viability
438 (see SI Appendix, Fig. S9E for a model). Due to the inefficient sister chromatid separation, MS-WGD
439 causes more skewed homologue distribution in the subsequent interphase than CF-WGD, often with
440 all four homologous chromosomes located on one side of the nucleus (SI Appendix, Fig. S9E-i). The
441 skewed homologue distribution persists until the entry into the first mitosis, when the separated four
442 centrosomes surround the chromosome mass from all sides (SI Appendix, Fig. S9E-ii). This
443 intracellular configuration causes a higher deviation in the centrosome-homologous centromere
444 distance after MS-WGD than CF-WGD, with some centrosomes located particularly distal from any
445 of the homologous centromeres. Our live-imaging suggests that this heterogeneity in the distance
446 from each centrosome to the homologous centromeres has a crucial impact on the efficiency of its
447 homologue capturing: A centrosome placed further than 10 μm from any homologous centromeres at
448 NEBD has a drastically higher chance of nullisomic segregation (Fig. 5F and SI Appendix, Fig. S6D).
449 Interestingly, this threshold distance corresponds well with the length that spindle microtubules can
450 reach during prometaphase in mammalian cells (47). Therefore, a centrosome is more likely to lose
451 to other centrosomes in the "competition" for homologous chromosomes when it is initially isolated

452 from homologous centromeres further than its microtubules can reach (SI Appendix, Fig. S9E-iii).
453 We found that the degree of the initial centrosomal isolation well explained the frequency of
454 subsequent nullisomic segregation (Fig. 5F and G). Moreover, the artificial sister chromatid
455 separation in MS-WGD significantly alleviated the skewed chromosome distribution and reduced
456 nullisomic segregation (Fig. 6 and SI Appendix, Fig. S8). These results demonstrate that the skewed
457 homologous chromosome arrangement resulting from inefficient sister chromatid separation is the
458 crucial cause of the higher prevalence of nullisomic chromosome segregation after MS-WGD (SI
459 Appendix, Fig. S9E-iv). In other words, sister chromatid separation contributes to "evening out" the
460 intranuclear distribution of homologous chromosomes, facilitating efficient centrosome-chromosome
461 interactions at mitosis in the next cell cycle, whose significance becomes evident in the geometric
462 condition of post-WGD cells.
463
464 The low prevalence of diplochromosomes in the first mitosis after MS-WGD (SI Appendix, Fig. S7I)
465 suggests that sister chromatids are mostly disjoined upon MS-WGD, as reported in other animal cells
466 (48). However, live imaging revealed that they failed to separate efficiently by a distance (Fig. 6C
467 and SI Appendix, Fig. S7C), in contrast to more efficient chromosome separation in the absence of a
468 spindle (so-called "C-anaphase") in plant cells (49). We found that precocious sister chromatid
469 disjunction induced their separation even during prometaphase, resulting in a further increase in their
470 distance during the subsequent MS-WGD (SI Appendix, Fig. S7H and 6C). Although the mechanisms
471 underlying the pre-anaphase separation remain unknown, we speculate that this precocious separation
472 helps further chromatid segregation observed during MS-WGD in RAD21- or Sororin-depleted cells.
473
474 While our results suggest that the frequent nullisomy caused by the skewed homologous chromosome
475 distribution is an important factor that limits the F1 cell viability after MS-WGD, the following facts
476 indicate the contributions of other unknown factors to limiting viability of MS-WGD cells: I) While

477 the transient RAD21-mAC depletion reduced the frequency of nullisomy after MS-WGD to the
478 equivalent level as that after CF-WGD (particularly in case of tripolar segregation; Fig. 6J), the F1
479 viability after MS-WGD with the transient RAD21-mAC depletion was still lower than that after CF-
480 WGD (Fig. 6K, L, 2F, and G). II) Moreover, CF-WGD progenies showed better survivability than
481 MS-WGD progenies even after bipolar chromosome segregation (Fig. 2G; supposed to be devoid of
482 frequent nullisomy). In this context, it would be beneficial to consider other issues arising from MS-
483 WGD beyond the aggravation of nullisomy. A recent study in C. elegans embryos reported that
484 artificially altering the developmentally programmed CF-WGD in intestinal cells to MS-WGD
485 compromised the expression of genes required for embryo growth (50). The study proposed that
486 differences in nuclear surface-to-volume ratio may have altered gene regulation between MS- and
487 CF-WGD. Another recent study reported MS-specific alterations in chromatin organization,
488 attributed to precocious mitotic exit and an abnormally high level of mitotic-specific histone H3
489 phosphorylation (51). Therefore, several independent principles, including the one found here, may
490 critically affect the more dysregulated characteristics of MS-derived cells.
491
492 Fates of post-WGD progenies beyond the F1 generation would be more complicated. We found that
493 the F1 population, whether from MS- or CF-WGD, included mononucleated and multinucleated
494 polyploids (Fig. 2E). Therefore, their intranuclear organization is expected to be more heterogeneous
495 and potentially cluttered than that immediately after WGD. Therefore, WGD route differences would
496 have direct effects only on the intranuclear organization and chromosome segregation patterns in the
497 first cell cycle. However, F1 cells derived from MS- and CF-WGD cells differed not only in the
498 frequency of nullisomy, but also in that of other types of copy number abnormalities, such as
499 monosomy or trisomy (SI Appendix, Fig. S4C). Therefore, the initial differences between MS- and
500 CF-WGD cells would be transmitted and have a long-term influence on the characteristics of their
501 progeny in the form of basal karyotypic profiles. Related to this point, it should be noted that the

502 frequency of copy number alterations may differ across chromosome species, whereas at least three
503 chromosome species (chromosomes 1, 9, and 17) with different sizes showed a similar trend in our
504 results. To accurately understand genome-wide trends in karyotypic alterations across different WGD
505 routes, single-cell genome-wide copy-number analysis would be a powerful approach in future
506 studies.
507
508 The impacts of differences in WGD routes on subsequent cell viability may also provide an important
509 clue to the control of post-WGD cell populations in cancer therapeutics. Recently, it has been pointed
510 out that anticancer drug treatment often causes artificial induction of WGD in tumors, potentially
511 causing the risk of recurrence through subsequent proliferation of these post-WGD progenies (2).
512 Since sister chromatid separation is a key factor affecting post-WGD cell proliferation, suppressing
513 it, for example, through topoisomerase II inhibitors (52) could be a potential approach to reduce the
514 risk of post-WGD cell proliferation. Our findings indicate the importance of understanding the
515 differential effects of WGD processes on subsequent cell fates for accurate comprehension of
516 principles of WGD-driven biological processes and their precise control.
517

518 **Materials and methods**

519

520 A detailed description of Materials and methods is provided in Supporting Text 2 in the SI Appendix.

521

522 *Cell culture and reagents*

523 Cell lines, plasmid vectors, or compounds and antibodies used in this study are listed in Dataset S1,
524 S2, or S3, respectively. Cell culture, nucleic acid transfection, WGD induction, or biochemical
525 analyses were conducted as detailed in SI Appendix, Supporting Text 2.

526

527 *Imaging*

528 All cell images were acquired using a TE2000, Ti, or Ti2 microscope (Nikon). Detailed information
529 on sample preparation, microscope equipment, or quantitative image analysis is provided in SI
530 Appendix, Supporting Text 2.

531

532 *Statistical analysis*

533 Analyses for significant differences between or among conditions were conducted as detailed in SI
534 Appendix, Supporting Text 2. Statistical significance was set at $p < 0.05$. *P*-values are indicated in
535 figures or the corresponding figure legends.

536

537

Acknowledgment

We are grateful to Masato Kanemaki, Gohta Goshima, and Kinya Yoda for reagents, Sarah McClelland, Koya Yoshizawa, Saori Takahashi and Ichiro Hiratani for valuable comments, and the NIC at Hokkaido University for microscopes. MI and GY are supported by JST SPRING, Grant Number JPMJSP2119. This work was supported by JSPS KAKENHI (Grant Numbers JP19KK0181, JP19H05413, JP19H03219, JPJSBP120193801, JP21K19244, JP22H04926, JP24K21956, JP24KK0139, and JP24K02017 to R.U.), the Princess Takamatsu Cancer Research Fund, the Kato Memorial Bioscience Foundation, the Orange Foundation, the Smoking Research Foundation, Daiichi Sankyo Foundation of Life Science, the Akiyama Life Science Foundation, the Hoansha Foundation, Sumitomo Electric Group CSR Foundation, and the Terumo Life Science Foundation to R.U. The authors declare no competing financial interests.

Author Contributions

Conceptualization, M.I., and R.U.; Methodology, M.I., G.Y., Y.T., and R.U.; Investigation, M.I.; Formal Analysis, M.I., and R.U.; Resources, M.I., G.Y., Y.T., and R.U.; Supervision, R.U.; Writing – Original Draft, R.U.; Writing – Review & Editing, M.I., and R.U.; Funding Acquisition, M.I., G.Y., Y.T., and R.U.

558 **Figure legends**

559

560 **Figure 1. Less efficient cell proliferation after MS-WGD than CF-WGD**

561 **(A)** A scheme of WGD induction. **(B)** An MS- or CF-WGD-induced cell, fixed at 4 h after WGD
562 induction. The centrosomes or DNA were stained with anti-Cep192 or DAPI, respectively. Insets
563 show 3x enlarged images of the centrosomes. Broken lines indicate cell contours. **(C)** Frequency of
564 nuclear numbers in WGD-induced cells at the first cell cycle. Pooled data from at least 235 cells from
565 three independent experiments. **(D)** Hoechst 33342-stained colonies formed after WGD induction.
566 The entire well views (left) or single colony images (right). Mock treatment control without WGD
567 induction on top (non-WGD). **(E)** Examples of DNA content distribution, quantified from Hoechst
568 33342 signal, in single colonies for each condition in D. Arrowheads indicate the estimated G1 DNA
569 content values in the exemplified colonies. Note that the DNA content of G1 populations varied
570 among colonies, reflecting their ploidy levels. See Supplemental Material S1 for histograms taken
571 from all colonies in each condition. **(F)** Ploidy levels of individual colonies, calculated by normalizing
572 their G1 DNA contents such that the average G1 DNA content of the diploid control was set to 2.
573 Each data point represents a single colony. At least 355 colonies from six replicates from three
574 independent experiments were analyzed for MS- or CF-WGD samples. Thirty-two colonies from
575 three independent experiments for diploid control. Colonies with normalized G1 DNA content of > 3
576 C were defined as "polyploid." **(G)** Number of polyploid colonies per well in each WGD condition.
577 Means ± s.e. of six replicates from three independent experiments (**$p < 0.01$, the Brunner-Munzel
578 test).

579

580 **Figure 2. Poorer survival of MS-WGD cells through multipolar chromosome segregation at the**
581 **first mitosis**

582 **(A)** A scheme of WGD induction and live imaging. **(B)** Time-lapse of H2B-mCherry cells during the
583 first mitosis after CF-WGD. Images were taken at 10-min intervals. The NEBD timing is set to 0 min.

584 White arrowheads indicate "mononucleated" daughter cells. The yellow arrow indicates a binucleated
585 cell formed through incomplete cytokinesis between two daughter cells. SI Appendix, Fig. S3B shows
586 MS-WGD cells. **(C)** Frequency of chromosome segregation polarity in Fig. 2B and SI Appendix, Fig.
587 S3B. Means ± s.e. of three independent experiments. At least 108 cells were analyzed in each
588 condition (p = 0.95, the Fisher exact test). **(D)** An example of the estimation of daughter cell DNA
589 content based on the segregation ratio of H2B-mCherry signal. For the demonstration, an identical
590 cell to the "tetrapolar" cell in B is shown. **(E)** Estimated DNA content (C-value) in individual F1 cells
591 in the live imaging. Data are sorted according to the prolife of the first mitosis (chromosome
592 segregation polarity and the presence or absence of daughter cell multinucleation) that formed the
593 corresponding F1 cells. At least 257 cells from three independent experiments. **(F, G)** Viability
594 (proportion of "divided" cells) of F1 cells, sorted by DNA content of individual F1 cells (F) or by the
595 polarity of chromosome segregation (G). Means ± s.e. of three independent experiments (n.s.: not
596 significant, ***p < 0.001, the Brunner-Munzel test). At least 55 or 28 cells were analyzed in each bin
597 (F) or polarity (G), respectively. Only mononucleated F1 cells were used for the quantification in G.
598

599 **Figure 3. More frequent nullisomic chromosome segregation occurs at the first mitosis after**
600 **MS-WGD than CF-WGD**

601 **(A, C, E)** Anaphase cells at the first mitosis after MS- or CF-WGD. The centrosomes, centromeres
602 of chromosome 9, and chromosomes were labeled by EGFP-GCP3, dCas9-EGFP with specific
603 sgRNA (C9-1), and H2B-mCherry, respectively, in A. Identical images with indications of the
604 centrosome positions are shown in SI Appendix, Fig. S4B. Genome loci on chromosome 1 (C) or
605 chromosome 17 (E) were stained with specific FISH probes. Chromosomes were stained with DAPI
606 in C and E. Yellow arrowheads indicate C9-1 foci or FISH signals. Broken lines indicate the contours
607 of chromosome masses. Orange arrows indicate chromosome masses devoid of the labeled
608 homologous chromosomes (nullisomy). The number of C9-1 foci or FISH signals in each
609 chromosome mass is indicated in the bottom panels. **(B, D, F)** Frequency of the segregated

610 chromosome masses devoid of any signals for chromosome 9 (B), 1 (D), or 17 (F). Means ± s.e. of
611 three independent experiments (***$p < 0.001$, the Brunner-Munzel test). At least 252, 116, or 172
612 segregated chromosome masses (presumptive daughter nuclei) were analyzed in each polarity in B,
613 D, or F, respectively. **(G, H)** Comparison between the model-predicted and empirical viability of
614 mononucleated (G) or binucleated (H) F1 cells. See *Materials and methods* for details of the model
615 prediction. The empirical data in G are identical to those in Fig. 2G (shown for direct comparison),
616 and those in H were obtained from at least 33 cells from three independent experiments.
617
618 **Figure 4. Skewed distribution of homologous centromeres in the first mitosis after MS-WGD**
619 **(A)** Cells at the entry into the first mitosis after MS- or CF-WGD. The centrosomes, centromeres of
620 chromosome 9, and chromosomes were labeled by EGFP-GCP3, dCas9-EGFP with specific sgRNA
621 (C9-1), and H2B-mCherry, respectively. **(B)** Histogram of inter-centromere distance in A. Six inter-
622 centromere distances among the 4 C9-1 foci were obtained from each cell. At least 414 C9-1
623 centromere combinations from at least 69 cells from three independent experiments (***$p < 0.001$,
624 the Welch's t-test). C9-1 combinations with their distance less than 2 μm (defined as "paired
625 centromeres") are indicated by the blue arrow. **(C)** Frequency of cells with paired C9-1 centromeres
626 in A. Means ± s.e. of three independent experiments (***$p < 0.001$, the Brunner-Munzel test). **(D)**
627 Left: An example of the inter-centromere angle quantification. For the demonstration, the identical
628 CF-WGD cell in A is shown. Right: Histogram of the angles between two C9-1 foci with regard to
629 the centroid of the whole-chromosome mass in A. At least 354 C9-1 combinations from at least 59
630 cells from three independent experiments were analyzed (***$p < 0.001$, the Welch's t-test). **(E)** Left:
631 Schematic images of the closest centrosome-centromere distance with skewed or more even
632 homologous centromere distributions. Right: Histogram of the distance from each centrosome to its
633 closest C9-1 focus in A. Four centrosome-centromere distances were obtained from an individual cell.
634 The centrosome-centromere combinations whose distances exceeded 10 μm (defined as "isolated
635 centrosomes") are indicated by the green arrow. At least 276 centrosome-centromere combinations

636 from at least 69 cells from three independent experiments were analyzed (***$p < 0.001$, the Welch's
637 t-test). **(F)** Standard deviation of the closest centrosome-centromere distances in each cell in A.
638 Asterisks indicate statistically significant difference between conditions (***$p < 0.001$, Welch's t-
639 test). **(G)** Frequency of isolated centrosomes in A. Means ± s.e. of three independent experiments
640 (***$p < 0.001$, the Brunner-Munzel test).
641
642 **Figure 5. Geometric isolation of centrosomes drives nullisomic chromosome segregation after**
643 **MS-WGD**

644 **(A)** Time-lapse images of H2B-mCherry, EGFP-GCP3, and dCas9-EGFP with C9-1 sgRNA
645 throughout the first mitosis after MS-WGD. Images were taken at 5-min intervals. The NEBD timing
646 is set to 0 min. The yellow circle indicates a chromosome mass devoid of any C9-1 foci. Individual
647 centrosomes were distinguished by labeling different letters (a-d). **(B)** The centrosome-centromere
648 distance of captured or uncaptured pairs in A. Means ± s.d. of at least 114 centrosome-centromere
649 pairs from 19 cells from five independent experiments. Asterisks indicate statistically significant
650 differences between conditions throughout mitosis (0-30 min after NEBD; ***$p < 0.001$, the Welch's
651 t-test). **(C)** The frequency of centrosome-centromere capturing, which was calculated for each bin of
652 the initial centrosome-centromere distance (schematized on the left). Three hundred four centrosome-
653 centromere pairs from 19 cells from five independent experiments were analyzed. **(D)** The time
654 course of the distance from each centrosome to its closest C9-1 focus (schematized on left) in the cell
655 shown in A. The asterisk indicates a centrosome that failed to capture any of the C9-1 foci. **(E)** The
656 initial distance (at NEBD) to the closest C9-1 focus from centrosomes that captured at least one C9-
657 1 focus (non-nullisomic) or those that did not capture any foci (nullisomic). Means ± s.d. of at least
658 14 centrosomes from 12 cells from five independent experiments (***$p < 0.001$, the Welch's t-test).
659 **(F)** The frequency of the centrosomes that failed to capture any C9-1, which was calculated for each
660 bin of the closest centrosome-centromere distance at NEBD (schematized on the left). At least 76
661 centrosomes from 19 cells from five independent experiments were analyzed. The number of

662 centrosomes failing to capture any C9-1 per total centrosomes in each bin is shown on top of each
663 graph bar. **(G)** Comparison between the model-predicted and empirical frequency of segregated
664 chromosome masses devoid of any C9-1 foci in tetrapolar chromosome segregation at the first mitosis
665 after MS- or CF-WGD. See *Materials and methods* for details of the model prediction. The empirical
666 data are identical to those in Fig. 3B (for the direct comparison). Means ± s.e. of three independent
667 experiments (***$p < 0.001$, the Brunner-Munzel test).
668
669 **Figure 6. Suppression of nullisomic homologue segregation at the first mitosis by artificial sister**
670 **chromatid separation upon MS-WGD**
671 **(A)** The schedule for AID2-mediated transient depletion of RAD21 before MS-WGD induction. **(B)**
672 Time-lapse of dCas9-EGFP with C9-1 sgRNA and chromosomes stained with SiR-DNA during MS-
673 WGD in RAD21-mAC cells treated with or without 5-Ph-IAA. Images were taken at 6-min intervals.
674 The time after the start of WGD induction was indicated. **(C)** Time course of inter-sister chromatid
675 distance in B. Means ± s.d. of at least 22 sister chromatid pairs from at least 11 cells from two
676 independent experiments (**$p < 0.01$, the Welch's t-test; tested at the last time point). **(D)** Cells at the
677 entry into the first mitosis after MS-WGD in RAD21-mAC cells treated with or without 5-Ph-IAA.
678 The centrosomes, C9-1 centromeres, and chromosomes were labeled by immunostaining of Cep192,
679 expression of dCas9-EGFP with a targeting sgRNA, and DAPI staining, respectively. **(E, H)**
680 Histogram of inter-centromere distance (E) or the distance from each centrosome to its closest C9-1
681 focus (H). At least 168 C9-1 combinations (E) or at least 112 centrosome-C9-1 combinations (H)
682 from at least 28 cells from three independent experiments were analyzed (p values of the Welch's t-
683 test are shown). **(F, I)** Frequency of cells with paired C9-1 centromeres (F) or frequency of isolated
684 centrosomes (I) in D. Means ± s.e. of three independent experiments (***$p < 0.001$, the Brunner-
685 Munzel test). **(G)** Angles between each two C9-1 foci with regard to the centroid of the whole-
686 chromosome mass. At least 168 C9-1 combinations from at least 28 cells from three independent
687 experiments were analyzed (*$p < 0.05$, the Welch's t-test). **(J)** Frequency of C9-1 nullisomic

688 chromosome segregation during anaphase at the first mitosis after MS-WGD with or without the
689 transient RAD21-mAC depletion. Means ± s.e. of three independent experiments (***$p < 0.001$, the
690 Brunner-Munzel test). At least 150 segregated chromosome masses from at least 50 cells from three
691 independent experiments were analyzed in each polarity. **(K, L)** Viability of F1 cells in live imaging
692 analysis after MS-WGD with or without the transient RAD21 depletion. Data are sorted by ploidy of
693 individual F1 cells (K) or the polarity of chromosome segregation at the first mitosis (L). Means ±
694 s.e. of three independent experiments (n.s.: not significant, ***$p < 0.001$, the Brunner-Munzel test).
695 At least 59 or 30 cells were analyzed in each bin (K) or polarity (L), respectively. Only mononucleated
696 F1 cells were used for the quantification in L.
697

References

1. Y. Van de Peer, E. Mizrachi, K. Marchal, The evolutionary significance of polyploidy. *Nature Reviews Genetics* **18**, 411-424 (2017).
2. P. J. Conway, J. Dao, D. Kovalskyy, D. Mahadevan, E. Dray, Polyploidy in Cancer: Causal Mechanisms, Cancer-Specific Consequences, and Emerging Treatments. *Mol Cancer Ther* **23**, 638-647 (2024).
3. G. S. Darmasaputra, L. M. van Rijnberk, M. Galli, Functional consequences of somatic polyploidy in development. *Development* **151** (2024).
4. T. Y. Lau, R. Y. C. Poon, Whole-Genome Duplication and Genome Instability in Cancer Cells: Double the Trouble. *Int J Mol Sci* **24** (2023).
5. N. Sanz-Gómez, M. González-Álvarez, J. De Las Rivas, G. de Cárcer, Whole-Genome Doubling as a source of cancer: how, when, where, and why? *Front Cell Dev Biol* **11**, 1209136 (2023).
6. H. Was *et al.*, Polyploidy formation in cancer cells: How a Trojan horse is born. *Seminars in Cancer Biology* **81**, 24-36 (2022).
7. A. C. Rios *et al.*, Essential role for a novel population of binucleated mammary epithelial cells in lactation. *Nat Commun* **7**, 11400 (2016).
8. S. H. Hsu *et al.*, MicroRNA-122 regulates polyploidization in the murine liver. *Hepatology* **64**, 599-615 (2016).
9. M. H. Soonpaa, K. K. Kim, L. Pajak, M. Franklin, L. J. Field, Cardiomyocyte DNA synthesis and binucleation during murine development. *Am J Physiol* **271**, H2183-2189 (1996).
10. R. Darp, M. A. Vittoria, N. J. Ganem, C. J. Ceol, Oncogenic BRAF induces whole-genome doubling through suppression of cytokinesis. *Nat Commun* **13**, 4109 (2022).
11. S. Soeda *et al.*, v-Src causes delocalization of Mklp1, Aurora B, and INCENP from the spindle midzone during cytokinesis failure. *Exp Cell Res* **319**, 1382-1397 (2013).
12. C. L. Rieder, H. Maiato, Stuck in division or passing through: what happens when cells cannot satisfy the spindle assembly checkpoint. *Dev Cell* **7**, 637-651 (2004).
13. M. Haschka, G. Karbon, L. L. Fava, A. Villunger, Perturbing mitosis for anti‐cancer therapy: is cell death the only answer? *EMBO reports* **19**, e45440 (2018).
14. D. A. Brito, C. L. Rieder, Mitotic Checkpoint Slippage in Humans Occurs via Cyclin B Destruction in the Presence of an Active Checkpoint. *Current Biology* **16**, 1194-1200 (2006).
15. G. Mondal *et al.*, Overexpression of Cdc20 leads to impairment of the spindle assembly checkpoint and aneuploidization in oral cancer. *Carcinogenesis* **28**, 81-92 (2007).
16. D. Schnerch *et al.*, BubR1 is frequently repressed in acute myeloid leukemia and its re-expression sensitizes cells to antimitotic therapy. *Haematologica* **98**, 1886-1895 (2013).
17. K. M.-F. Sze, Y.-P. Ching, D.-Y. Jin, I. Oi-Lin Ng, Association of MAD2 expression with mitotic checkpoint competence in hepatoma cells. *Journal of Biomedical Science* **11**, 920-927 (2004).
18. X. Wang *et al.*, Significance of MAD2 expression to mitotic checkpoint control in ovarian cancer cells.

735 *Cancer Res* **62**, 1662-1668 (2002).
736 19. N. Sakurikar, J. M. Eichhorn, T. C. Chambers, Cyclin-dependent kinase-1 (Cdk1)/cyclin B1 dictates
737 cell fate after mitotic arrest via phosphoregulation of antiapoptotic Bcl-2 proteins. *J Biol Chem* **287**,
738 39193-39204 (2012).
739 20. M. Horiuchi *et al.*, The tyrosine kinase v-Src causes mitotic slippage by phosphorylating an inhibitory
740 tyrosine residue of Cdk1. *J Biol Chem* **293**, 15524-15537 (2018).
741 21. S. Mazzi, L. Lordier, N. Debili, H. Raslova, W. Vainchenker, Megakaryocyte and polyploidization.
742 *Experimental Hematology* **57**, 1-13 (2018).
743 22. N. Sanz-Gómez *et al.*, Squamous differentiation requires G2/mitosis slippage to avoid apoptosis. *Cell*
744 *Death Differ* **27**, 2451-2467 (2020).
745 23. Y. Aylon, M. Oren, p53: Guardian of ploidy. *Molecular Oncology* **5**, 315-323 (2011).
746 24. Neil J. Ganem *et al.*, Cytokinesis Failure Triggers Hippo Tumor Suppressor Pathway Activation. *Cell*
747 **158**, 833-848 (2014).
748 25. L. L. Fava *et al.*, The PIDDosome activates p53 in response to supernumerary centrosomes. *Genes Dev*
749 **31**, 34-45 (2017).
750 26. A. Crockford *et al.*, Cyclin D mediates tolerance of genome-doubling in cancers with functional p53.
751 *Ann Oncol* **28**, 149-156 (2017).
752 27. T. A. Potapova, C. W. Seidel, A. C. Box, G. Rancati, R. Li, Transcriptome analysis of tetraploid cells
753 identifies cyclin D2 as a facilitator of adaptation to genome doubling in the presence of p53. *Mol Biol*
754 *Cell* **27**, 3065-3084 (2016).
755 28. A. Y. Kuznetsova *et al.*, Chromosomal instability, tolerance of mitotic errors and multidrug resistance
756 are promoted by tetraploidization in human cells. *Cell Cycle* **14**, 2810-2820 (2015).
757 29. N. J. Ganem, S. A. Godinho, D. Pellman, A mechanism linking extra centrosomes to chromosomal
758 instability. *Nature* **460**, 278-282 (2009).
759 30. M. Kwon *et al.*, Mechanisms to suppress multipolar divisions in cancer cells with extra centrosomes.
760 *Genes Dev* **22**, 2189-2203 (2008).
761 31. W. T. Silkworth, I. K. Nardi, L. M. Scholl, D. Cimini, Multipolar spindle pole coalescence is a major
762 source of kinetochore mis-attachment and chromosome mis-segregation in cancer cells. *PLoS One* **4**,
763 e6564 (2009).
764 32. N. C. Baudoin *et al.*, Asymmetric clustering of centrosomes defines the early evolution of tetraploid
765 cells. *Elife* **9** (2020).
766 33. T. Boveri, *Zur frage der entstehung maligner tumoren* (Gustav Fischer, 1914).
767 34. C. Yang *et al.*, Rapid proliferation of daughter cells lacking particular chromosomes due to multipolar
768 mitosis promotes clonal evolution in colorectal cancer cells. *Cell Cycle* **11**, 2650-2659 (2012).
769 35. D. Gisselsson *et al.*, When the genome plays dice: circumvention of the spindle assembly checkpoint
770 and near-random chromosome segregation in multipolar cancer cell mitoses. *PLoS One* **3**, e1871
771 (2008).
772 36. D. Gisselsson *et al.*, Generation of trisomies in cancer cells by multipolar mitosis and incomplete

773 cytokinesis. *Proc Natl Acad Sci U S A* **107**, 20489-20493 (2010).
774 37. A. W. Duncan *et al.*, Frequent Aneuploidy Among Normal Human Hepatocytes. *Gastroenterology* **142**,
775 25-28 (2012).
776 38. S. V. Bernhard, S. Gemble, R. Basto, Z. Storchova, "Experimental Approaches to Generate and Isolate
777 Human Tetraploid Cells" in Polyploidy: Methods and Protocols, Y. Van de Peer, Ed. (Springer US,
778 New York, NY, 2023), 10.1007/978-1-0716-2561-3_20, pp. 391-399.
779 39. Y. Uetake, G. Sluder, Cell cycle progression after cleavage failure: mammalian somatic cells do not
780 possess a "tetraploidy checkpoint". *J Cell Biol* **165**, 609-615 (2004).
781 40. F. Meitinger *et al.*, Control of cell proliferation by memories of mitosis. *Science* **383**, 1441-1448 (2024).
782 41. H. Ma *et al.*, Multicolor CRISPR labeling of chromosomal loci in human cells. *Proceedings of the*
783 *National Academy of Sciences* **112**, 3002-3007 (2015).
784 42. D. Gerlich *et al.*, Global Chromosome Positions Are Transmitted through Mitosis in Mammalian Cells.
785 *Cell* **112**, 751-764 (2003).
786 43. A. Yesbolatova *et al.*, The auxin-inducible degron 2 technology provides sharp degradation control in
787 yeast, mammalian cells, and mice. *Nat Commun* **11**, 5701 (2020).
788 44. V. J. Goyanes, J. B. Schvartzman, Insights on diplochromosome structure and behaviour. *Chromosoma*
789 **83**, 93-102 (1981).
790 45. S. Rankin, N. G. Ayad, M. W. Kirschner, Sororin, a Substrate of the Anaphase- Promoting Complex, Is
791 Required for Sister Chromatid Cohesion in Vertebrates. *Molecular Cell* **18**, 185-200 (2005).
792 46. J. Schmitz, E. Watrin, P. Lénárt, K. Mechtler, J.-M. Peters, Sororin Is Required for Stable Binding of
793 Cohesin to Chromatin and for Sister Chromatid Cohesion in Interphase. *Current Biology* **17**, 630-636
794 (2007).
795 47. M. Piehl, L. Cassimeris, Organization and dynamics of growing microtubule plus ends during early
796 mitosis. *Mol Biol Cell* **14**, 916-925 (2003).
797 48. C. L. Rieder, R. E. Palazzo, Colcemid and the mitotic cycle. *J Cell Sci* **102 (Pt 3)**, 387-392 (1992).
798 49. A.-M. Lambert, The role of chromosomes in anaphase trigger and nuclear envelope activity in spindle
799 formation. *Chromosoma* **76**, 295-308 (1980).
800 50. L. M. van Rijnberk *et al.*, Endomitosis controls tissue-specific gene expression during development.
801 *PLOS Biology* **20**, e3001597 (2022).
802 51. S. Gemble *et al.*, Mitotic slippage causes nuclear instability in polyploid cells. *bioRxiv*
803 10.1101/2025.07.21.665898, 2025.2007.2021.665898 (2025).
804 52. C. S. Downes, A. M. Mullinger, R. T. Johnson, Inhibitors of DNA topoisomerase II prevent chromatid
805 separation in mammalian cells but do not prevent exit from mitosis. *Proc Natl Acad Sci U S A* **88**, 8895-
806 8899 (1991).
807

Figure 1

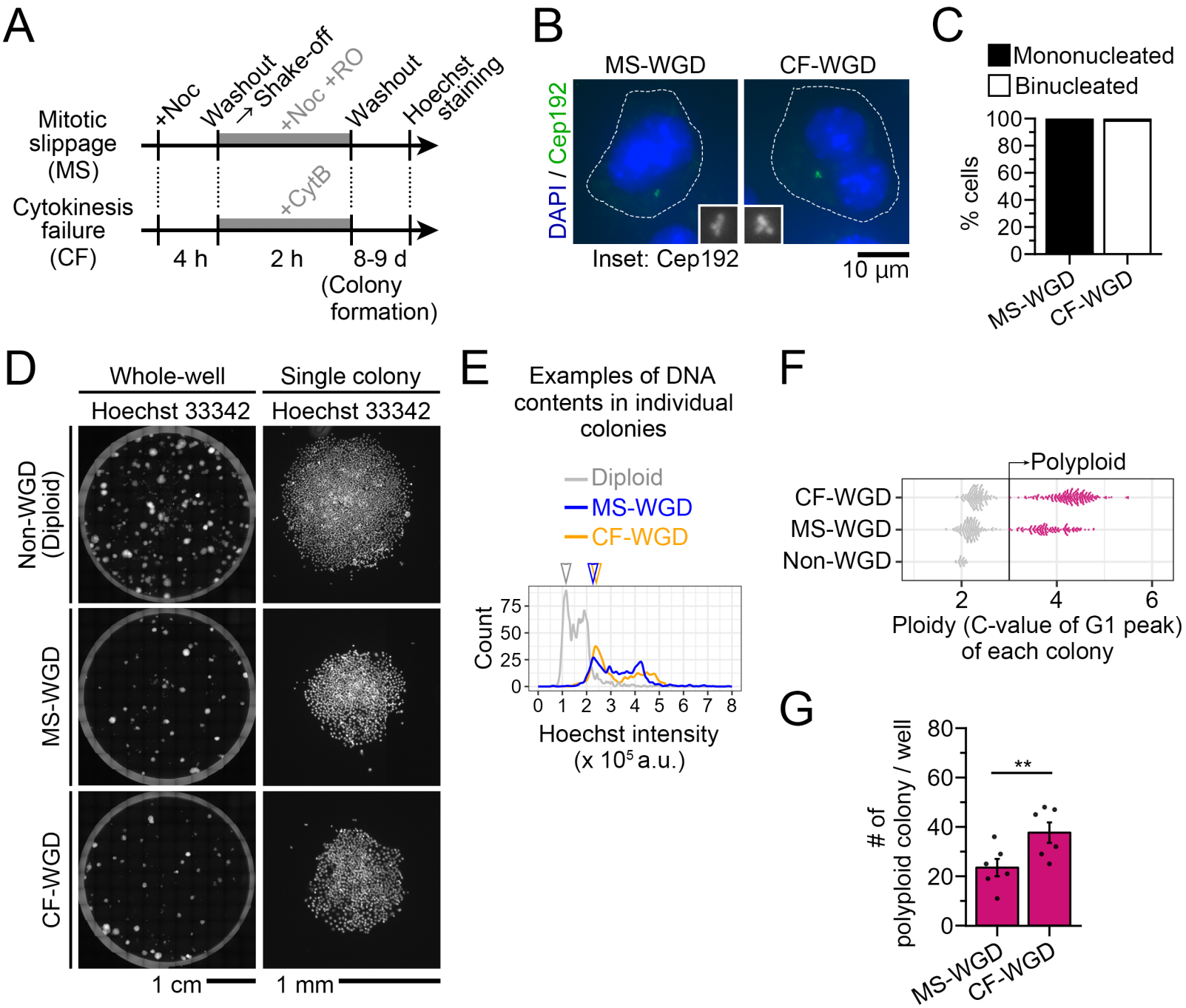
A
Mitotic slippage (MS)
Cytokinesis failure (CF)
+Noc
Washout → Shake-off
+Noc +RO
Washout
Hoechst staining
+CytB
4 h
2 h
8-9 d (Colony formation)
B
MS-WGD
CF-WGD
DAPI / Cep192
Inset: Cep192
10 µm
C
Mononucleated
Binucleated
% cells
100
80
60
40
20
0
MS-WGD
CF-WGD
D
Whole-well
Single colony
Hoechst 33342
Hoechst 33342
Non-WGD (Diploid)
MS-WGD
CF-WGD
1 cm
1 mm
E
Examples of DNA contents in individual colonies
Diploid
MS-WGD
CF-WGD
Count
75
50
25
0
0 1 2 3 4 5 6 7 8
Hoechst intensity (x 10⁵ a.u.)
F
Polyploid
CF-WGD
MS-WGD
Non-WGD
2
4
6
Ploidy (C-value of G1 peak) of each colony
G
# of polyploid colony / well
80
60
40
20
0
**
MS-WGD
CF-WGD

Figure 2

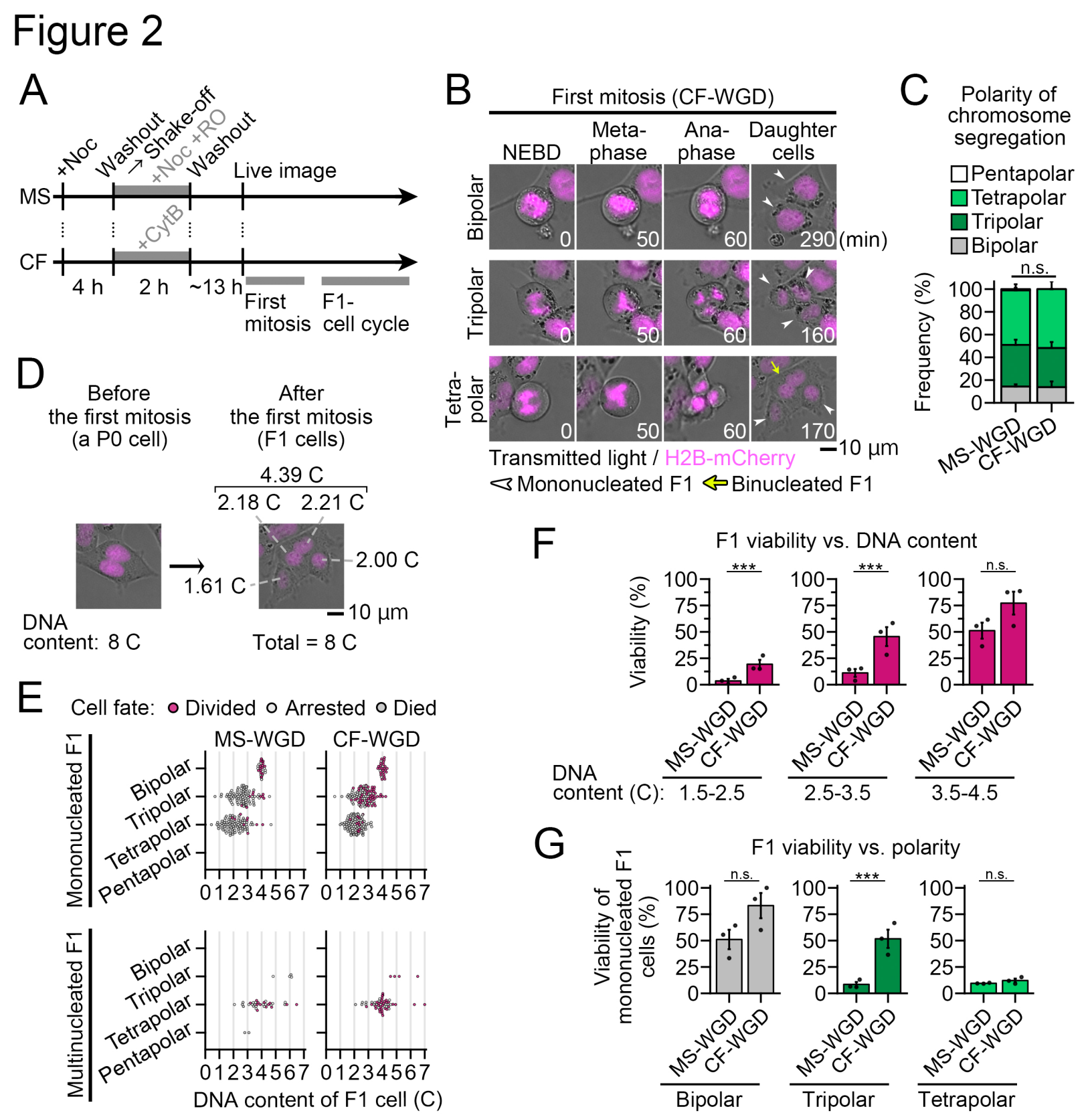
A
+Noc
Washout
Shake-off
+Noc +RO
Washout
Live image
MS
+CytB
CF
4 h
2 h
~13 h
First mitosis
F1-cell cycle
B
First mitosis (CF-WGD)
NEBD
Meta-phase
Ana-phase
Daughter cells
Bipolar
Tripolar
Tetra-polar
0
50
60
290
160
170
(min)
10 µm
Transmitted light / H2B-mCherry
Mononucleated F1
Binucleated F1
C
Polarity of chromosome segregation
Pentapolar
Tetrapolar
Tripolar
Bipolar
n.s.
Frequency (%)
100
80
60
40
20
0
MS-WGD
CF-WGD
D
Before the first mitosis (a P0 cell)
After the first mitosis (F1 cells)
4.39 C
2.18 C
2.21 C
2.00 C
1.61 C
10 µm
DNA content: 8 C
Total = 8 C
E
Cell fate: Divided Arrested Died
MS-WGD
CF-WGD
Mononucleated F1
Multinucleated F1
Bipolar
Tripolar
Tetrapolar
Pentapolar
0 1 2 3 4 5 6 7
DNA content of F1 cell (C)
F
F1 viability vs. DNA content
Viability (%)
***
n.s.
DNA content (C):
1.5-2.5
2.5-3.5
3.5-4.5
G
F1 viability vs. polarity
Viability of mononucleated F1 cells (%)
Bipolar
Tripolar
Tetrapolar

Figure 3

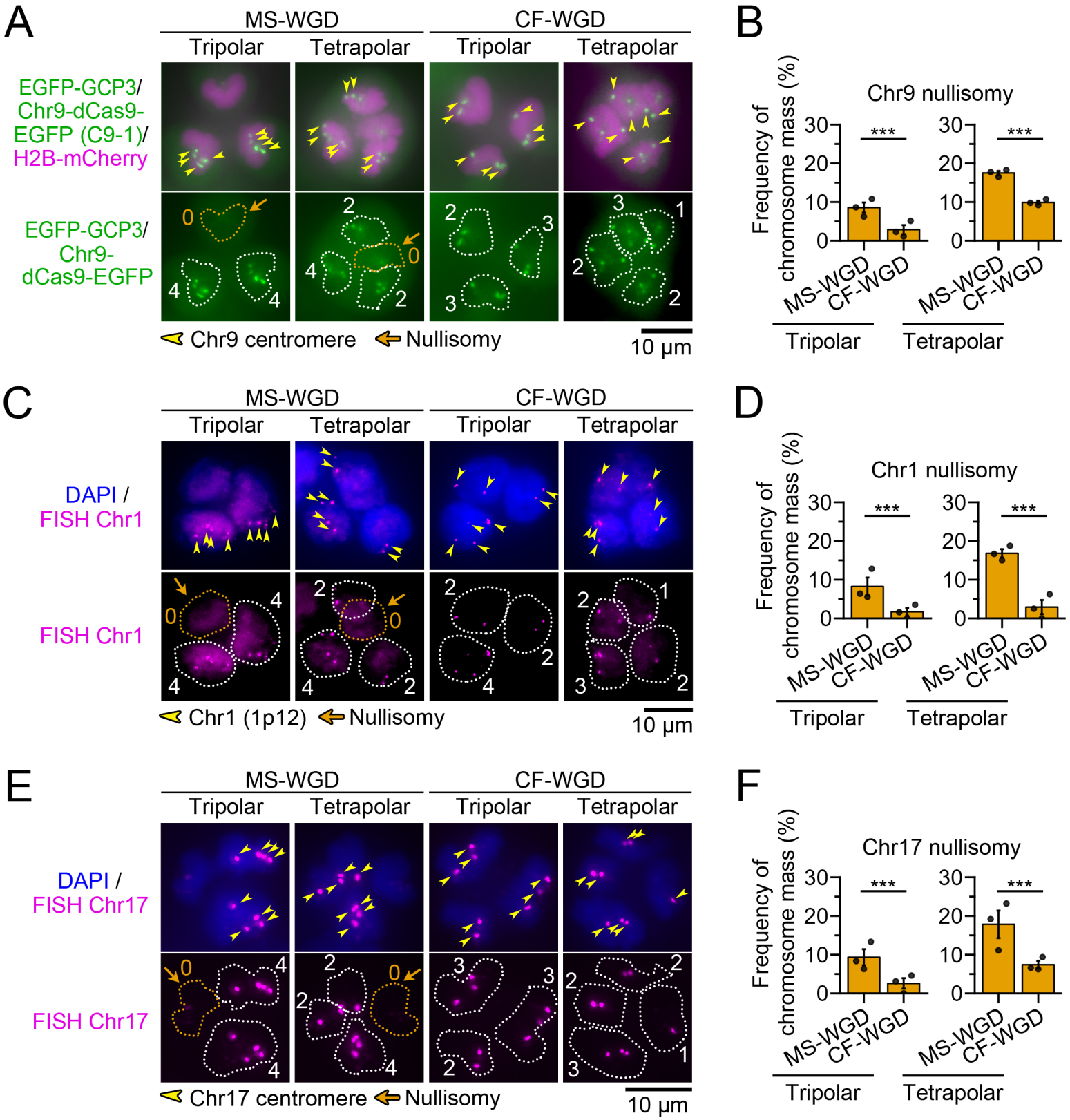
A
MS-WGD
CF-WGD
Tripolar
Tetrapolar
EGFP-GCP3/
Chr9-dCas9-
EGFP (C9-1)/
H2B-mCherry
EGFP-GCP3/
Chr9-
dCas9-EGFP
Chr9 centromere
Nullisomy
10 μm
B
Chr9 nullisomy
Frequency of chromosome mass (%)
***
MS-WGD
CF-WGD
Tripolar
Tetrapolar
C
DAPI /
FISH Chr1
FISH Chr1
Chr1 (1p12)
D
Chr1 nullisomy
E
DAPI /
FISH Chr17
FISH Chr17
Chr17 centromere
F
Chr17 nullisomy
G
F1 viability (Mononucleated)
Viability (%)
Model prediction
Empirical data
H
F1 viability (Binucleated from tetrapolar division)

Figure 4

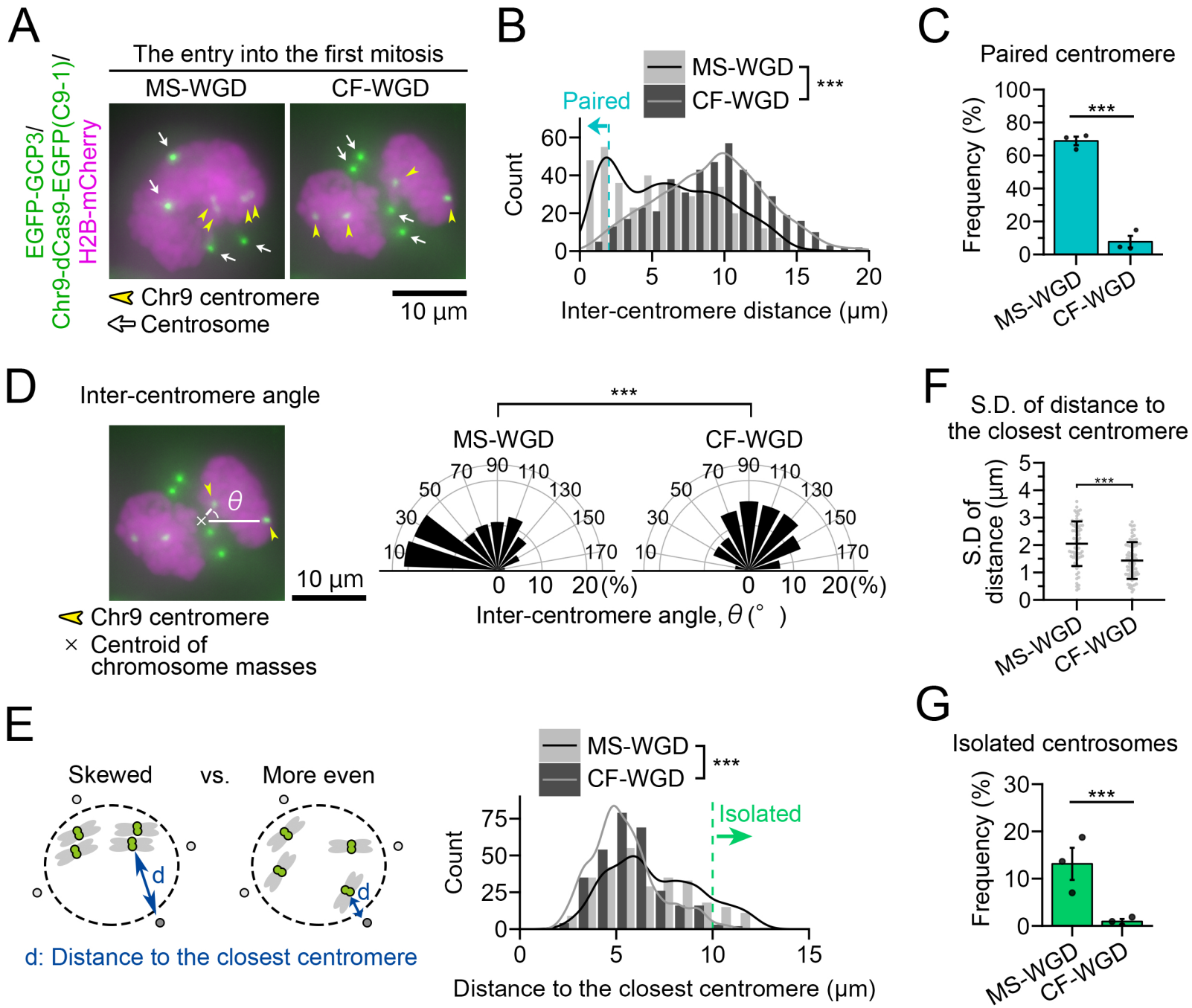
A
The entry into the first mitosis
MS-WGD
CF-WGD
EGFP-GCP3/
Chr9-dCas9-EGFP(C9-1)/
H2B-mCherry
Chr9 centromere
Centrosome
10 μm
B
MS-WGD
CF-WGD
***
Paired
Count
Inter-centromere distance (μm)
C
Paired centromere
Frequency (%)
***
MS-WGD
CF-WGD
D
Inter-centromere angle
θ
10 μm
Chr9 centromere
Centroid of chromosome masses
***
MS-WGD
CF-WGD
(%)
Inter-centromere angle, θ (°)
F
S.D. of distance to the closest centromere
S.D of distance (μm)
***
MS-WGD
CF-WGD
E
Skewed
vs.
More even
d
d: Distance to the closest centromere
MS-WGD
CF-WGD
***
Isolated
Count
Distance to the closest centromere (μm)
G
Isolated centrosomes
Frequency (%)
***
MS-WGD
CF-WGD

Figure 5

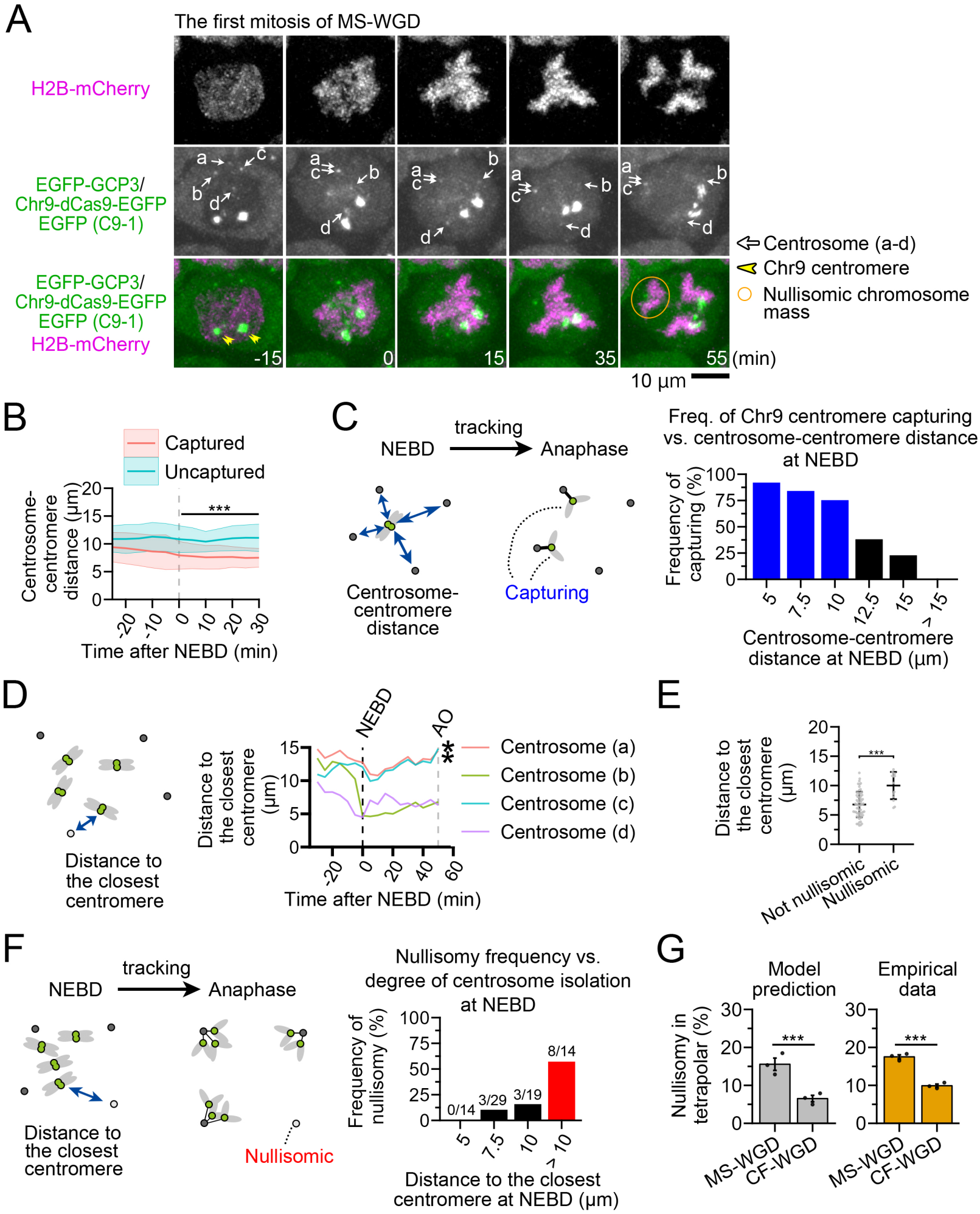
A
The first mitosis of MS-WGD
H2B-mCherry
EGFP-GCP3/
Chr9-dCas9-EGFP
EGFP (C9-1)
EGFP-GCP3/
Chr9-dCas9-EGFP
EGFP (C9-1)
H2B-mCherry
a
b
c
d
-15
0
15
35
55 (min)
10 μm
Centrosome (a-d)
Chr9 centromere
Nullisomic chromosome mass
B
Captured
Uncaptured
Centrosome-centromere distance (μm)
***
Time after NEBD (min)
C
NEBD
tracking
Anaphase
Centrosome-centromere distance
Capturing
Freq. of Chr9 centromere capturing vs. centrosome-centromere distance at NEBD
Frequency of capturing (%)
Centrosome-centromere distance at NEBD (μm)
D
Distance to the closest centromere
NEBD
AO
**
Distance to the closest centromere (μm)
Centrosome (a)
Centrosome (b)
Centrosome (c)
Centrosome (d)
Time after NEBD (min)
E
Distance to the closest centromere (μm)
***
Not nullisomic
Nullisomic
F
NEBD
tracking
Anaphase
Distance to the closest centromere
Nullisomic
Nullisomy frequency vs. degree of centrosome isolation at NEBD
Frequency of nullisomy (%)
0/14
3/29
3/19
8/14
Distance to the closest centromere at NEBD (μm)
G
Model prediction
Empirical data
Nullisomy in tetrapolar (%)
***
MS-WGD
CF-WGD

Figure 6

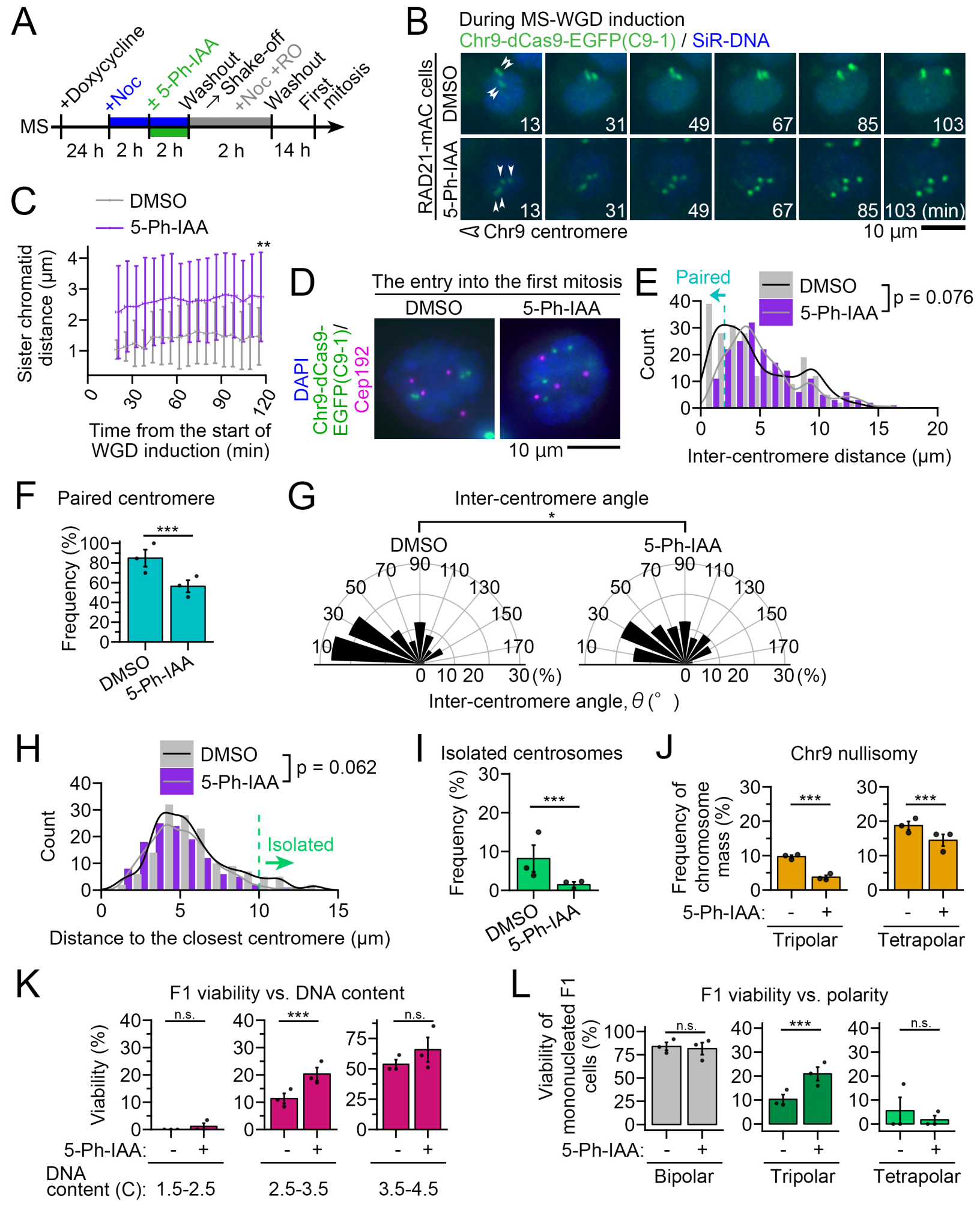
A
+Doxycycline
+Noc
± 5-Ph-IAA
Washout
→ Shake-off
+Noc +RO
Washout
First mitosis
MS
24 h
2 h
2 h
2 h
14 h
B
During MS-WGD induction
Chr9-dCas9-EGFP(C9-1) / SiR-DNA
RAD21-mAC cells
DMSO
5-Ph-IAA
13
31
49
67
85
103
103 (min)
Chr9 centromere
10 μm
C
DMSO
5-Ph-IAA
Sister chromatid distance (μm)
Time from the start of WGD induction (min)
D
The entry into the first mitosis
DMSO
5-Ph-IAA
DAPI
Chr9-dCas9-EGFP(C9-1)/
Cep192
10 μm
E
Paired
DMSO
5-Ph-IAA
p = 0.076
Count
Inter-centromere distance (μm)
F
Paired centromere
Frequency (%)
DMSO
5-Ph-IAA
G
Inter-centromere angle
DMSO
5-Ph-IAA
Inter-centromere angle, θ (°)
H
DMSO
5-Ph-IAA
p = 0.062
Isolated
Count
Distance to the closest centromere (μm)
I
Isolated centrosomes
Frequency (%)
DMSO
5-Ph-IAA
J
Chr9 nullisomy
Frequency of chromosome mass (%)
5-Ph-IAA:
Tripolar
Tetrapolar
K
F1 viability vs. DNA content
Viability (%)
5-Ph-IAA:
DNA content (C):
1.5-2.5
2.5-3.5
3.5-4.5
L
F1 viability vs. polarity
Viability of mononucleated F1 cells (%)
5-Ph-IAA:
Bipolar
Tripolar
Tetrapolar